

Developmentally programmed germ cell remodelling by endodermal cell cannibalism

Yusuff Abdu¹, Chelsea Maniscalco¹, John M. Heddleston², Teng-Leong Chew² and Jeremy Nance^{1,3,4}

Primordial germ cells (PGCs) in many species associate intimately with endodermal cells, but the significance of such interactions is largely unexplored. Here, we show that *Caenorhabditis elegans* PGCs form lobes that are removed and digested by endodermal cells, dramatically altering PGC size and mitochondrial content. We demonstrate that endodermal cells do not scavenge lobes PGCs shed, but rather, actively remove lobes from the cell body. CED-10 (Rac)-induced actin, DYN-1 (dynamin) and LST-4 (SNX9) transiently surround lobe necks and are required within endodermal cells for lobe scission, suggesting that scission occurs through a mechanism resembling vesicle endocytosis. These findings reveal an unexpected role for endoderm in altering the contents of embryonic PGCs, and define a form of developmentally programmed cell remodelling involving intercellular cannibalism. Active roles for engulfing cells have been proposed in several neuronal remodelling events, suggesting that intercellular cannibalism may be a more widespread method used to shape cells than previously thought.

Primordial germ cells (PGCs) are segregated from somatic cells in the early embryo, where they undergo unique regulation to preserve their fate as precursors to the germ line. For example, PGCs in many species suppress transcription to prevent the initiation of somatic differentiation programs^{1,2}. Another conserved but poorly understood aspect of PGC development is an intimate association with endodermal cells. PGC–endodermal interactions have been described in a wide variety of invertebrate and vertebrate animals. For instance, mouse PGCs are sequestered in the embryonic hindgut before continuing their migration to the genital ridge³; tunicate PGCs are found among endodermal strand cells prior to their migration to the rudimentary gonad⁴; and *Drosophila* and *C. elegans* PGCs are carried into the embryo by attaching to gastrulating endodermal cells^{5,6}. Aside from these roles for endoderm in positioning PGCs, it remains unknown whether endodermal cells influence PGCs in other ways. Using transmission electron microscopy, it was observed that *C. elegans* PGCs transiently extend large lobes into adjacent endodermal cells⁷. However, a role for PGC lobes, as well as their fate, has never been established. Here, we show that endodermal cells actively remove and digest PGC lobes to dramatically remodel PGC size and content, and we identify a molecular mechanism resembling vesicle endocytosis that mediates this form of intercellular cannibalism.

RESULTS

PGC lobes form autonomously and are digested by endodermal cells

We examined PGC lobe formation and fate in living embryos expressing germ cell-specific membrane-targeted mCherry (mCh-Mem^{PGC})⁸. The embryo contains two PGCs, called Z2 and Z3. Prior to the 1(1/2)-fold stage of embryogenesis, Z2 and Z3 transitioned from a roughly spherical shape to a dumbbell shape by extending a large lobe, which just after forming embedded into the surface of an adjacent endodermal cell (Fig. 1a,b and Supplementary Videos 1 and 2). PGC lobes were similar in volume to the cell body but lacked a nucleus. To determine whether endodermal cells are needed for PGCs to form lobes, we examined endoderm-less *end-1 end-3* mutants⁹. PGCs are often found on the surface of *end-1 end-3* embryos, as endoderm is required for PGC gastrulation⁵. Even when in this ectopic location, PGCs formed lobes at a comparable embryonic stage (10/10 embryos) (Fig. 1d,d'). Isolated PGCs cultured from dissociated embryos also formed lobes (9/9 cells; Fig. 1e,e' and Supplementary Video 3). Thus, PGC lobe formation is an autonomous process that does not require interactions with other cells.

PGC lobes are no longer present when embryos hatch⁷, but it is unknown whether they are resorbed back into the PGC cell body or lost. The volume of PGCs in L1 larvae ($232 \pm 39 \mu\text{m}^3$) was

¹Helen L. and Martin S. Kimmel Center for Biology and Medicine at the Skirball Institute of Biomolecular Medicine, NYU School of Medicine, New York, New York 10016, USA. ²Advanced Imaging Center, Janelia Research Campus, Howard Hughes Medical Institute, Ashburn, Virginia 20147, USA. ³Department of Cell Biology, NYU School of Medicine, New York, New York 10016, USA.

⁴Correspondence should be addressed to J.N. (e-mail: Jeremy.Nance@med.nyu.edu)

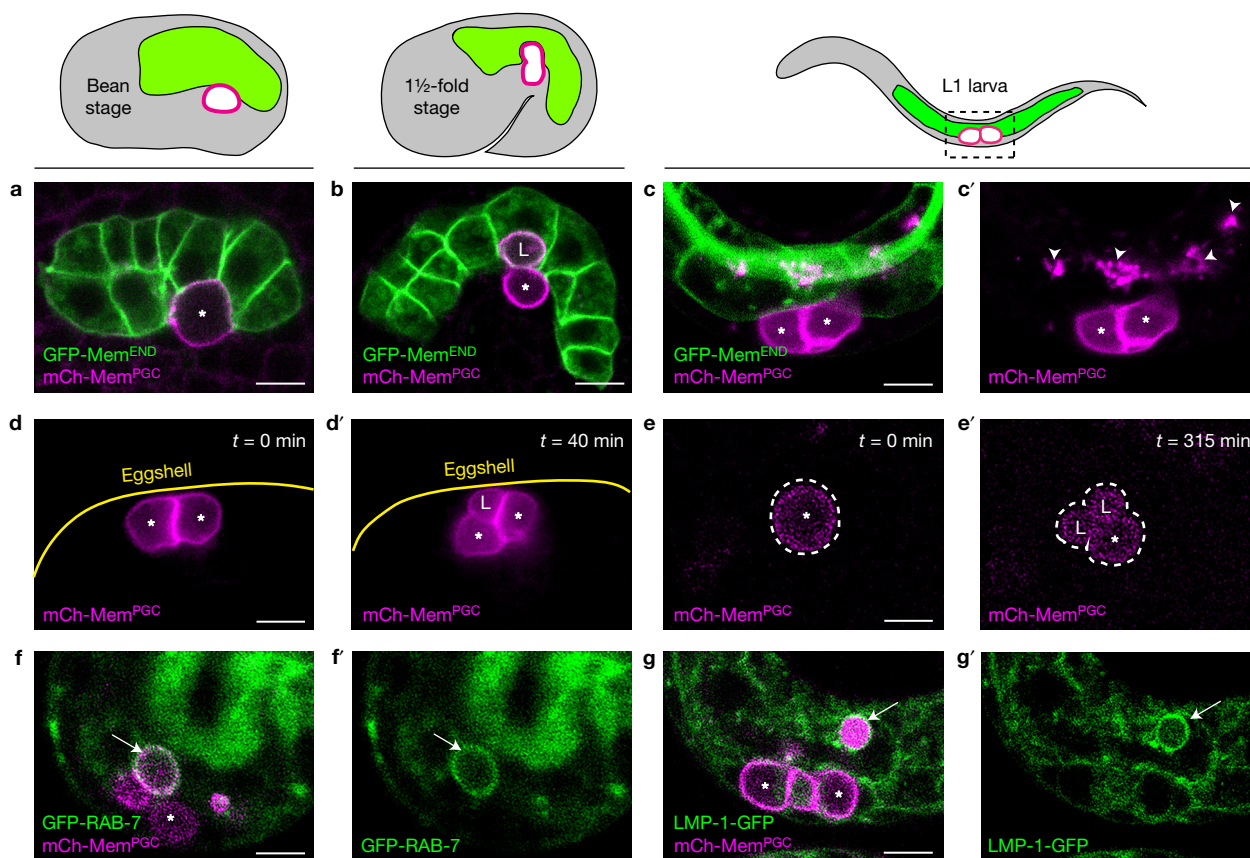


Figure 1 PGC lobes form autonomously and are digested by endodermal cells. (a) PGC and endoderm prior to lobe formation (bean stage); only one PGC is visible in the focal plane. (b) A PGC after lobe formation (1 1/2-fold embryo). The lobe (L) has embedded into the endoderm. (c,c') PGCs in L1 larvae; PGC lobe debris (arrowheads) is present within adjacent endodermal cells. (d,d') Time-lapse stills of PGCs on the surface of an *end-1 end-3*

mutant embryo before (d) and after (d') forming lobes. (e,e') A single PGC (dashed outline) in cell culture before a lobe forms (e) and after a lobe forms and bifurcates (e'); L, lobes. Stills taken from Supplementary Video 3. (f,f') GFP-RAB-7 (arrow) marking the surface of a lobe in a late embryo. (g,g') Lobe debris is marked with LMP-1-GFP (arrow). Asterisks mark PGC cell body. Scale bars, 5 μ m.

less than half that of embryonic PGCs that had not yet formed lobes ($555 \pm 36 \mu\text{m}^3$), and comparable to the main cell body of PGCs that had formed lobes ($213 \pm 26 \mu\text{m}^3$) (Fig. 2j), suggesting that lobes and their contents are lost. Further supporting lobe loss, red-fluorescent debris appeared within adjacent endodermal cells of L1 larvae expressing mCh-Mem^{PGC} (Fig. 1c,c' and Supplementary Fig. 1a,a'). Markers of late endosomes (GFP-RAB-7) and lysosomes (LMP-1-GFP) accumulated around red-fluorescent debris (Fig. 1f–g'), indicating that debris represents PGC lobe remnants that are being digested within endodermal cells.

Lobe loss remodels PGC contents and eliminates many mitochondria

To determine whether lobe debris contains PGC cellular components, we followed the fate of two organelles: P granules and mitochondria. P granules are germ cell-specific organelles that bind the PGC nuclear periphery (Fig. 2a)¹⁰. Although the majority of P granules remained attached to the nucleus and therefore stayed in the cell body, a subset of P granules (marked with PGL-1-RFP) moved from the nuclear periphery into lobes in most embryos (31/38 embryos; Fig. 2b and Supplementary Video 4), and L1 larvae expressing PGL-1-RFP contained red-fluorescent debris within endodermal

cells that were adjacent to the PGCs (Fig. 2c). We labelled PGC mitochondria using germ cell-specific mCherry-tagged MOMA-1 (mCh-MOMA-1^{PGC}), which is an outer mitochondrial membrane protein¹¹. A large fraction of mCh-MOMA-1^{PGC} localized to PGC lobes (Fig. 2d,e and Supplementary Video 5), and mCh-MOMA-1^{PGC} was present within endodermal cells adjacent to the PGCs in L1 larvae (Fig. 2f). Lobe loss resulted in a substantial reduction in mitochondria, as measured by the volume of PGC cell bodies occupied by mCh-MOMA-1^{PGC} in early embryos versus L1 larvae (Fig. 2k). We stained embryos with dyes shown to report on *C. elegans* mitochondrial membrane potential (TMRE) as well as oxidant levels (MitoSOX) to determine whether PGC mitochondria are different from those present in other cells (Supplementary Fig. 2)^{12,13}. PGC mitochondria showed similar membrane potential to mitochondria in other cell types (Fig. 2g,l). However, PGC mitochondria stained strongly with MitoSOX compared with mitochondria in most other cell types (Fig. 2h,i,l and Supplementary Fig. 2a), indicating that PGC mitochondria produce high levels of oxidants relative to most other cells. Together, these findings show that PGC lobes and their contents are shed or removed, taken up by endodermal cells, and digested. The loss of PGC lobes results in a marked remodelling of PGC size and cytoplasmic contents—some components such as P granules become

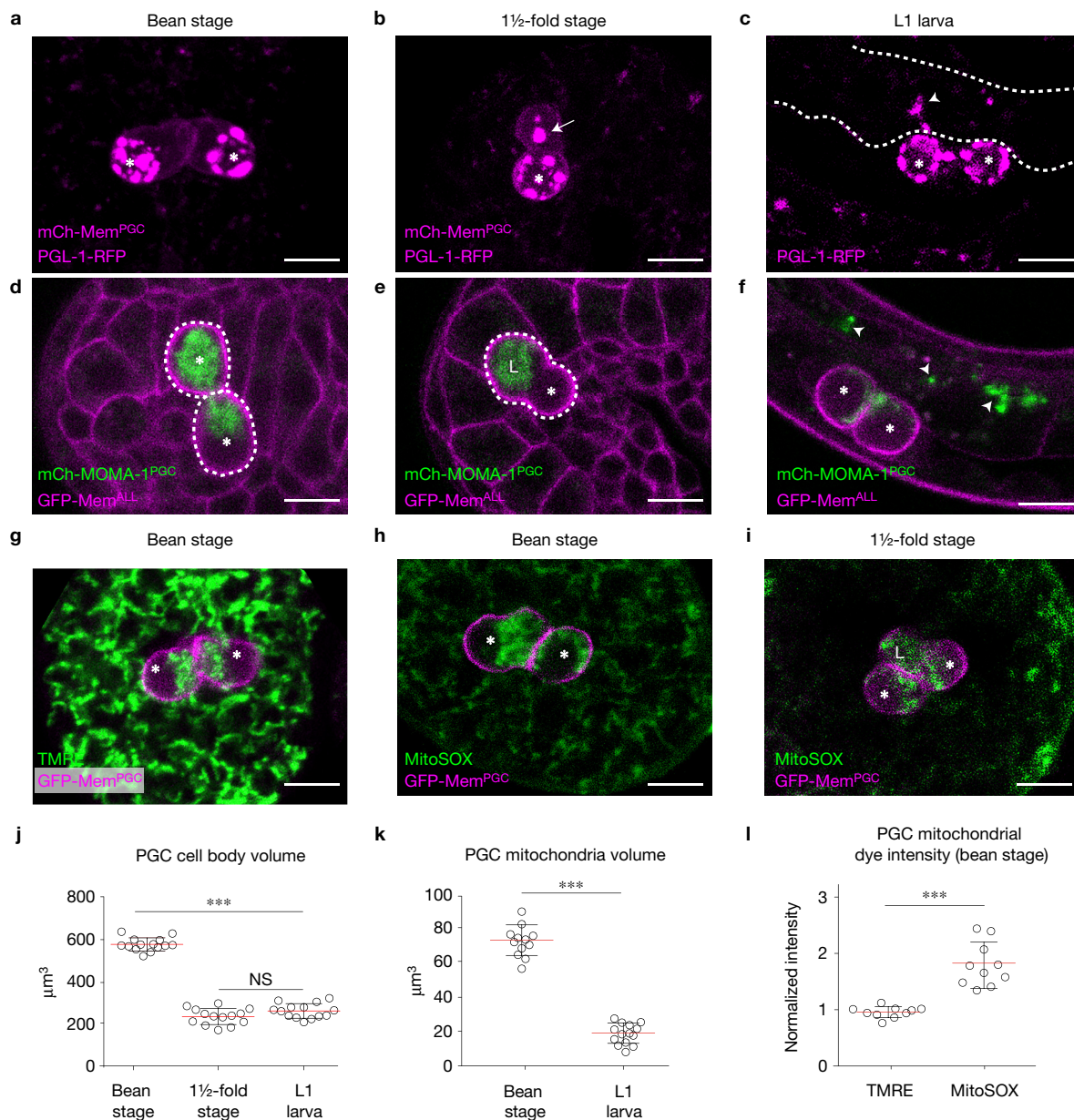


Figure 2 Lobe loss remodels PGC contents. (**a–c**) P granules localize to the nuclear periphery prior to lobe formation (**a**). Some P granules move into lobes (**b**, arrow) and are digested by endodermal cells (**c**, arrowhead; dashed lines indicate endoderm). **a,b** are from Supplementary Video 4. (**d–f**) PGC mitochondria (dashed outline indicates PGC membrane) before (**d**) and after (**e**) lobe formation, and as debris within endodermal cells in L1 (**f**, arrowheads). **d,e** are from Supplementary Video 5. (**g**) Mitochondrial membrane potential dye TMRE labels mitochondria in PGCs and soma at equal levels. (**h,i**) Compared with levels in soma, mitochondrial oxidant dye MitoSOX labels PGC mitochondria strongly before (**h**) and after (**i**) lobes (L) form. (**j**) Quantification of PGC cell body volume (bean, $n=14$; 1(1/2)-fold,

$n=14$; L1, $n=14$ from 1 out of 3 independent experiments; source data for repeat experiments are provided in Supplementary Table 3). (**k**) Quantification of mitochondria loss (bean stage, $n=12$ embryos; L1, $n=14$ L1 larvae from 1 out of 2 independent experiments; source data for repeat experiments are provided in Supplementary Table 3). (**l**) Quantification of fluorescence intensity of TMRE ($n=10$ embryos) and MitoSOX ($n=10$ embryos) labelling in PGC mitochondria normalized to average intensity levels in the soma. Data shown are from 1 out of 2 independent experiments. Source data for repeat experiments are provided in Supplementary Table 3. Mean (red bar) \pm s.d. is shown. Scale bars, 5 μ m. *** $P < 0.001$, unpaired Student's *t*-test. Asterisks mark PGC cell body.

more concentrated, whereas other components such as oxidant-rich mitochondria are largely depleted.

PGC lobe removal is a developmentally regulated event

We visualized the fate of individual lobes using lattice light-sheet microscopy¹⁴, which allowed us to rapidly acquire three-dimensional

image stacks and optically 'freeze' late embryos as they rotated within the eggshell. After lobes formed and embedded into the endoderm, they bifurcated one or more times to form smaller embedded lobes. Eventually, the smaller lobes appeared to detach from the PGC cell body and move into endodermal cells before rapidly condensing into debris. These events required 140 ± 20 min ($n=18$) following

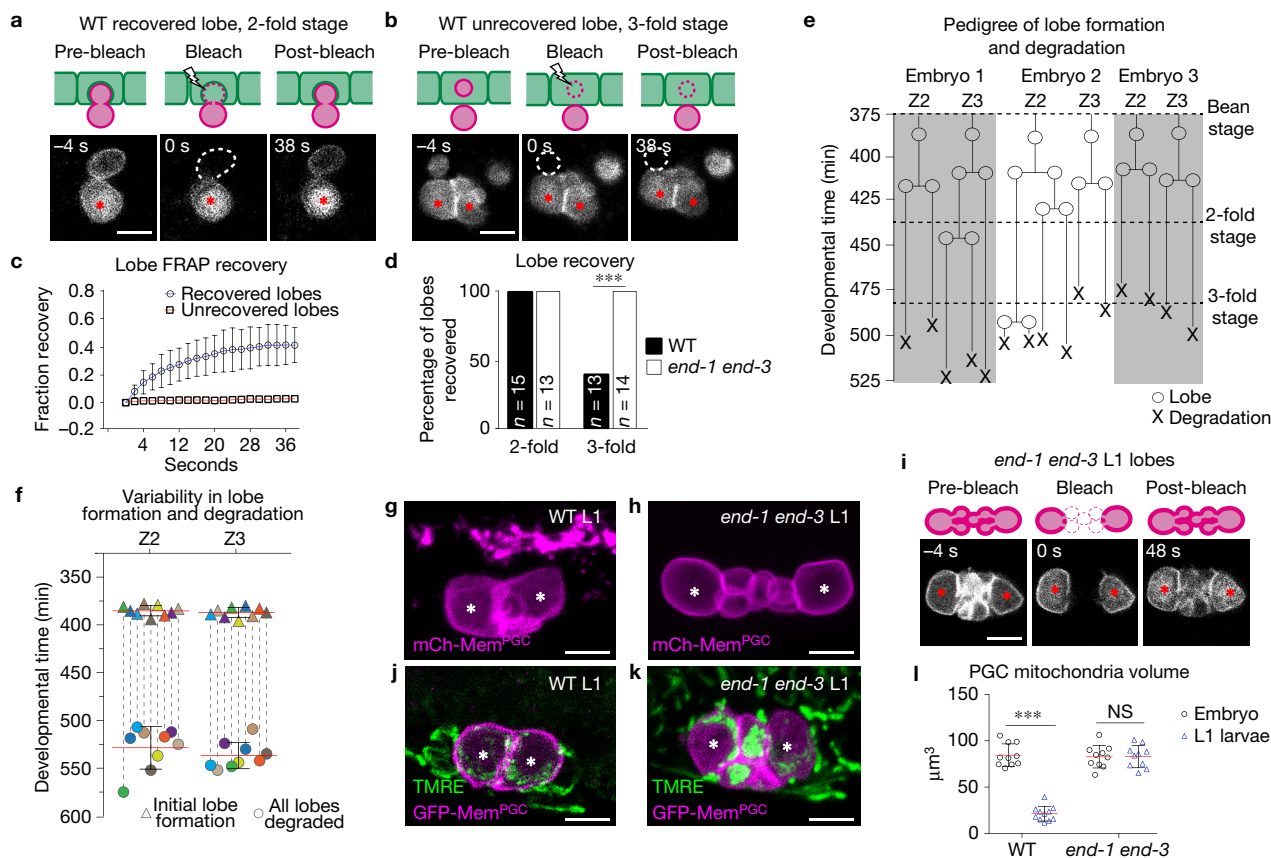


Figure 3 Endodermal cells actively remove PGC lobes. (a,b) FRAP of mCh-Mem^{PGC} in PGC lobes in 2-fold (a) and 3-fold (b) stage wild-type (WT) embryos; photobleached region is dashed. (c) Quantification of FRAP in 3-fold embryos showing examples of recovered and unrecovered lobes ($n=10$ lobes in 10 embryos each class, mean \pm s.d. shown). (d) Percentage of lobe recovery in WT and *end-1 end-3* 2-fold and 3-fold embryos ($***P < 0.001$, Fisher's exact test). (e) Pedigrees tracking Z2 and Z3 lobe formation and degradation in three representative embryos. Lobe formation or bifurcation (circle) and degradation (cross) are indicated. (f) Z2 and Z3 lobe formation and degradation in nine embryos. Dashed vertical lines connect initial lobe formation (triangle) to final degradation of the lobe

descendants (circle) from a single PGC ($n=9$ embryos). (g,h) PGC lobes are digested in WT L1 larvae (g), but persist in *end-1 end-3* L1 larvae (h). (i) FRAP of all persistent lobes in *end-1 end-3* L1 larvae (recovery in 14/14 L1). (j,k) PGCs retain higher mitochondrial content in *end-1 end-3* L1 larvae (k) compared with WT L1 larvae (j). (l) Quantification of mitochondria retention (WT: $n=10$ embryos, 11 L1 larvae; *end-1 end-3*: $n=10$ embryos, 10 L1 larvae). Data shown are from 1 out of 2 independent experiments. Source data for repeat experiments are provided in Supplementary Table 3. Mean \pm s.d. shown. Scale bars, 5 μm . $***P < 0.001$, unpaired Student's *t*-test. NS, not significant. Asterisks mark PGC cell body.

the appearance of the initial lobe. We used fluorescence recovery after photobleaching (FRAP) of mCh-Mem^{PGC} to determine whether lobes actually detach from the PGC cell body or remain connected by a thin membrane bridge; photobleached attached lobes should recover fluorescence by diffusion from the unbleached cell body. Lobes always recovered fluorescence when photobleached in 2-fold embryos—a stage before PGC debris appears within endodermal cells (Fig. 3a,c,d). However, only 38% of lobes recovered fluorescence when photobleached in 3-fold embryos—a stage when PGC debris is visible within endodermal cells (Fig. 3b,c,d). These results indicate that lobes undergo scission and detach from the PGC cell body before endodermal cells digest them.

On the basis of our light-sheet videos, we constructed complete pedigrees of PGC lobes in nine embryos. The exact timing and pattern of lobe bifurcation and degradation varied between PGCs and between embryos, but always occurred within a defined developmental period (Fig. 3e,f). Unexpectedly, all of the lobes derived from one PGC began to degrade before any of the lobes from the other PGC did so ($n=9$

embryos, 40 lobes; Fig. 3e). However, either PGC (Z2 or Z3) was equally capable of having its lobes detach and degrade first (Z2 first: 5 embryos, 23 lobes; Z3 first: 4 embryos, 17 lobes). These findings show that lobe scission is a developmentally regulated event and probably involves intercellular communication.

Endodermal cells actively remove PGC lobes

Endodermal cells could phagocytose lobes that PGCs shed, or alternatively, could actively remove lobes still attached to the PGC body. To distinguish these possibilities, we determined whether lobes remain connected to the PGC cell body in *end-1 end-3* mutants. PGC lobes in *end-1 end-3* L1 larvae persisted (Fig. 3g,h), recovered fluorescence in FRAP experiments (Fig. 3d,i), and filled with a rhodamine dextran dye that was uncaged only in the PGC cell body (8/8 larvae; Supplementary Fig. 3). These findings show that lobes remain connected to the PGC body when endoderm is absent, indicating that endodermal cells normally remove and digest lobes from PGCs. We confirmed that lack of lobe removal results in a failure

to remodel PGC contents by examining TMRE-stained mitochondria in *end-1 end-3* embryos. Mitochondria still enriched in lobes in *end-1 end-3* embryos (Fig. 3k). However, because lobes remained attached to the cell body, the PGC volume occupied by mitochondria in *end-1 end-3* was similar in embryos and L1 larvae, in contrast to wild type (Fig. 3j,l). Hereafter, we refer to this form of live cell remodelling as ‘cannibalism’ to distinguish it from other remodelling events that occur via the shedding and subsequent phagocytosis of cellular debris.

Endodermal cell CED-10 (Rac) induces actin formation to promote lobe scission

We examined genes that function in cell or cell fragment uptake to determine whether they are needed for PGC lobe cannibalism. *ced-10* (*Rac1*), which encodes a Rho GTPase that regulates actin organization, functions in engulfing cells to mediate the phagocytosis of cell corpses¹⁵. *ced-10* null mutants arrest at early stages of embryogenesis¹⁶. In viable *ced-10(n1993)* hypomorphic mutant embryos, lobes formed normally and embedded properly into endodermal cells (Fig. 4a,b). However, a subset of PGC lobes persisted in 100% of *ced-10(n1993)* L1 larvae ($n = 115$; Supplementary Table 1), and PGC debris within endodermal cells was greatly reduced (Fig. 4a,b,e). Many of the persistent lobes in *ced-10(n1993)* L1 larvae (96/104 lobes in 44 L1) maintained a thin membrane attachment to the PGC cell body (Fig. 4b,b’), and 100% of persistent lobes recovered from photobleaching ($n = 19$ larvae; Fig. 4c), indicating that *ced-10* is required for lobe scission. Persistent lobes in *ced-10(n1993)* mutants were rescued by expressing *ced-10(+)* in endodermal cells (Fig. 4d and Supplementary Fig. 4c), and analysis of rare intra-endodermal mosaic embryos indicated that *ced-10(+)* activity is required within cells where lobe scission occurs ($n = 11$ L1 larvae; Supplementary Fig. 4a-b). Mosaic L1 larvae obtained using a *ced-10(tm597)* null allele showed a similar persistent lobe phenotype, further supporting a specific role for *ced-10* in lobe scission (Supplementary Fig. 4d). In most *ced-10(n1993)* mutants, persistent lobes eventually disappeared by the end of the first larval stage (36/52 late L1), perhaps due to an alternative mechanism that removes PGC lobes in larvae or mechanical shearing as germ cells begin to divide.

ced-10 is required for the formation of an actin halo that surrounds cell corpses to drive their engulfment¹⁷. We examined YFP-tagged actin in endodermal cells (YFP-ACT-5^{END}) to determine whether actin also accumulates around lobes. In light-sheet videos, we did not detect YFP-ACT-5^{END} around lobes as they initially embedded into endodermal cells. However, YFP-ACT-5^{END} enriched transiently at the necks of PGC lobes (Fig. 4f) just prior to the visible separation of PGC lobes from the cell body (Fig. 4h; 15/15 lobes in 6 embryos). In light-sheet videos of *ced-10* mutants, only 13% of lobe necks accumulated YFP-ACT-5^{END} (3/23 lobes in 6 embryos; Fig. 4g); these lobes underwent scission and were digested by endodermal cells, whereas lobes that failed to accumulate actin always persisted (Fig. 4h). These findings suggest that *ced-10*-dependent actin accumulation around lobe necks promotes lobe scission.

CED-10 (Rac) functions with dynamin and LST-4 (SNX9) to promote lobe scission

In the process of cell corpse engulfment, *ced-10* functions with two partially redundant pathways: the *ced-1/6/7* (‘Draper/Ced-1’)

pathway helps to recognize cell corpses, whereas the *ced-2/5/12* (‘CrkII/Dock180/Elmo1’) pathway activates CED-10 (ref. 18). Mutations in genes within the *ced-1/6/7* pathway (*ced-1*, *ced-7*, *nrf-5*, *tr-52*), the *ced-2/5/12* pathway (*ced-2*, *ced-5*), or both pathways (*ced-1;ced-2* and *ced-7;ced-5*) did not cause PGC lobes to persist in L1 larvae (Supplementary Table 1), indicating that *ced-10* functions in PGC lobe scission in a different context than it does in cell corpse engulfment. We performed a forward genetic screen to find genes that function with *ced-10* to mediate lobe scission. One mutant, *xn45*, closely resembled *ced-10* mutants in phenotype: most *xn45* L1 larvae contained persistent PGC lobes (70% of L1, $n = 121$) that remained connected to the PGC body, as revealed by FRAP experiments (Fig. 5a,b,e and Supplementary Fig. 5c). We identified *xn45* as a splice donor mutation in *lst-4*, which encodes a SNX9-family sorting nexin (Supplementary Fig. 5a,b,d). Mammalian SNX9 can tubulate membranes and has a role in vesicle scission^{19–21}, and *lst-4* contributes to phagosome sealing and maturation^{22–25}. Endodermally expressed YFP-LST-4 accumulated at lobe necks and rescued the persistent PGC lobe phenotype of *lst-4* mutants (0/90 embryos had persistent lobes, versus 40/46 *lst-4* mutant siblings; Fig. 5c,d). Thus, *lst-4*, like *ced-10*, functions within endodermal cells to promote lobe scission.

LST-4 contains an amino-terminal SH3 domain; a PX domain; and a carboxy-terminal BAR domain, which is disrupted by the *xn45* mutation (Supplementary Fig. 5d). The SH3 domain of LST-4 and SNX9 binds dynamin^{18,20}. Given that both SNX9 and dynamin can deform membranes and function in vesicle scission²¹, we asked whether dynamin (encoded by *dyn-1*) is required for PGC lobe scission. Because *dyn-1* mutants arrest at the end of embryogenesis²⁶, we examined PGC lobes in age-matched (~3-fold) wild-type, *dyn-1* mutant, or *dyn-1*; *dyn-1(+)* rescued embryos. In all wild-type and *dyn-1*; *dyn-1(+)* rescued embryos, most or all lobes had been removed. By contrast, in 62% of *dyn-1* mutant embryos, all lobes persisted (Fig. 5f,g and Supplementary Table 2), and FRAP experiments revealed that persistent lobes remained connected to the cell body (16/16 embryos; Fig. 5j). YFP-DYN-1 expressed in endoderm accumulated at lobe necks and rescued the persistent lobe defects of *dyn-1* mutants (3/39 embryos had persistent lobes, versus 25/30 *dyn-1* mutant siblings), consistent with a local requirement for lobe scission (Fig. 5h,i). Similar to actin, in light-sheet videos YFP-DYN-1^{END} accumulation occurred shortly before lobe degradation commenced (6/6 embryos, 15/15 lobes; Fig. 6a). YFP-DYN-1^{END} still accumulated at lobe necks in light-sheet videos of *ced-10* mutants (6/6 embryos, 28/28 lobes; Fig. 6a), indicating that dynamin localization does not require lobe-neck actin. Similarly, YFP-ACT-5 accumulated at lobe necks in *dyn-1* mutants, which were examined at a single point during the 3-fold stage (YFP-ACT-5 localized to at least one lobe neck in 7/28 *dyn-1* mutant embryos compared with 6/21 rescued *dyn-1*; *dyn-1(+)* embryos; Fig. 6c). We conclude that endodermal dynamin is required for PGC lobe scission, and that dynamin and actin can accumulate at lobe necks independently.

In addition to binding dynamin, the SNX9 SH3 domain also interacts with N-WASP to regulate actin polymerization during vesicle endocytosis^{27–30}. Therefore, we asked whether *lst-4* is needed for actin and dynamin to concentrate at lobe necks. Because the *lst-4(xn45)* mutation is not predicted to disrupt the SH3 domain, we examined CFP-DYN-1^{END} and YFP-ACT-5^{END} in *lst-4(RNAi)* L1 larvae,

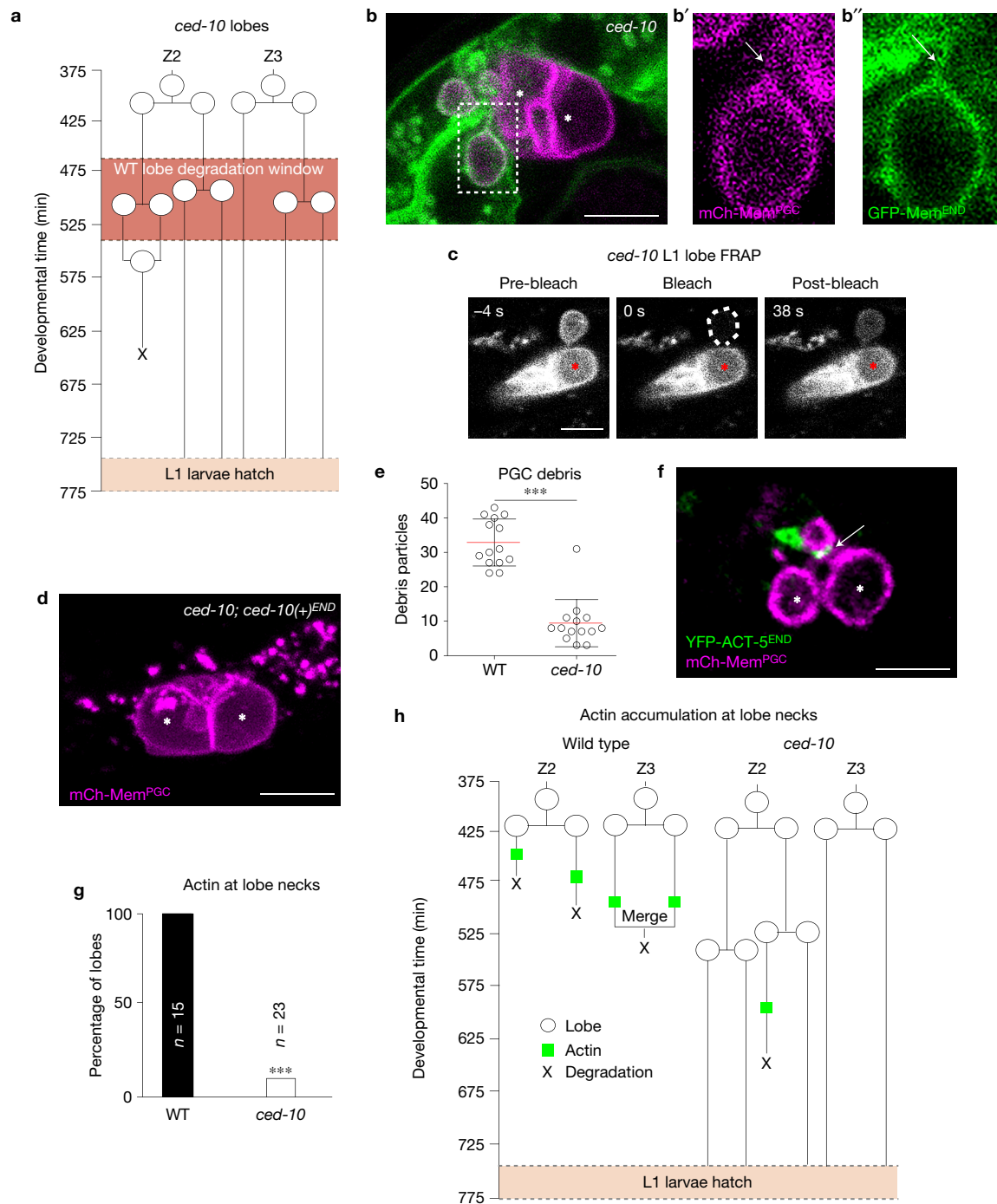


Figure 4 Endodermal cell CED-10 induces actin formation to promote lobe scission. **(a)** Pedigree of lobe formation (circle) and degradation (cross) in a *ced-10* mutant. **(b–b'')** Persistent lobes in a *ced-10* L1 larva; membrane stalk connecting lobe to cell body is indicated by arrows **b'** and **b''** are magnifications of the outlined area in **b**. **(c)** FRAP of persistent lobes in *ced-10* L1 larva (recovery in 19/19 L1); photobleached region is dashed. **(d)** Endoderm-specific expression of *ced-10(+)* (from *xnEx375*) rescues *ced-10(n1993)* persistent lobes ($n = 14$ L1 larvae). **(e)** Number of PGC debris particles in WT and *ced-10* mutants (mean \pm s.d.,

$***P < 0.001$, Student's unpaired *t*-test). $n = 14$ L1 larvae from 1 out of 3 independent experiments. Source data for repeat experiments are provided in Supplementary Table 3. **(f)** Localization of YFP-ACT-5^{END} (arrow) at a lobe neck. **(g)** Percentage of lobes with actin localization events in WT and *ced-10* mutants ($***P < 0.001$, Fisher's exact test). $n = 15$ lobes in 6 embryos (WT) and $n = 23$ lobes in 6 embryos (*ced-10*) acquired from light-sheet data. **(h)** Pedigree of lobes and lobe-neck actin appearance in WT and *ced-10* mutants. Scale bars, 5 μ m. Asterisks mark PGC cell body.

which showed a stronger persistent lobe phenotype than *lst-4* mutants (Fig. 5b and Supplementary Fig. 5c). In control 3-fold stage embryos examined at a single point, when only a subset of lobes are undergoing

scission, YFP-ACT-5^{END} and CFP-DYN-1^{END} localized to 23% and 28% of lobe necks, respectively (Fig. 6d). Some lobe necks contained either YFP-ACT-5^{END} or CFP-DYN-1^{END}, whereas the two proteins

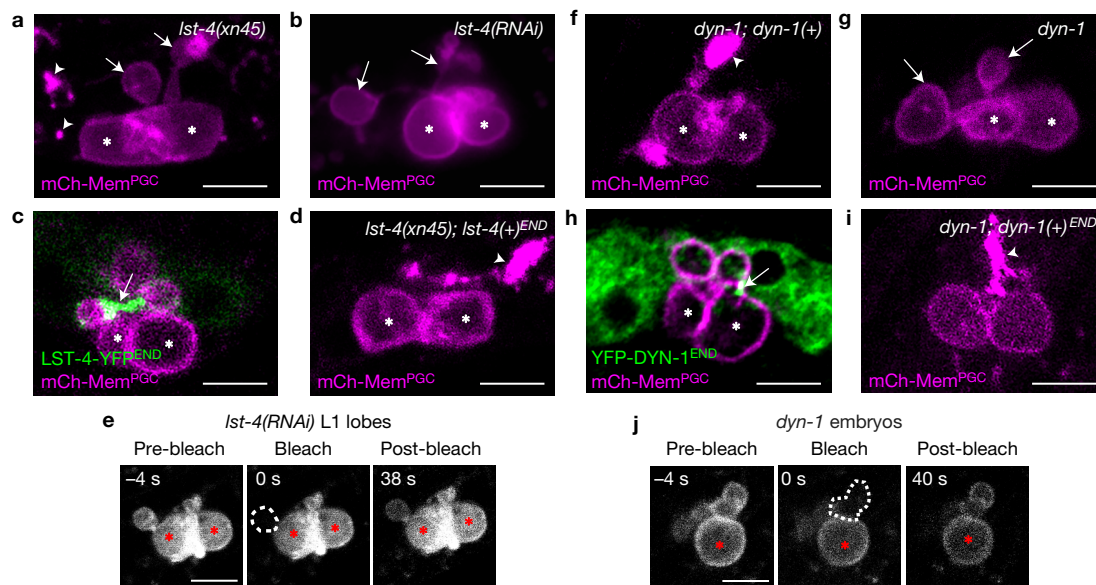


Figure 5 Endodermal LST-4 and dynamin act to promote lobe scission. (a,b) Persistent lobes (arrows) in *Ist-4(xn45)* mutants (a; arrowheads, lobe debris) and *Ist-4(RNAi)* (b) L1 larvae. (c) Localization of LST-4-YFP^{END} (arrow) at a lobe neck. (d) Rescue of persistent lobes in *Ist-4(xn45)* L1 by LST-4-YFP^{END}; arrowhead indicates debris (persistent lobes in 0/90 L1, compared with 40/40 siblings lacking LST-4-YFP^{END} from 3 independent experiments). (e) FRAP of persistent lobes in *Ist-4(RNAi)* L1 larvae (recovery in 15/15 L1 from 3 independent experiments); photobleached region

is dashed. (f,g) *dyn-1* mutant (g) and rescued (f) embryos; persistent lobes in *dyn-1* embryos indicated by arrows, debris in rescued embryos marked by arrowhead. (h) YFP-DYN-1^{END} localizes to lobe necks (arrow). (i) YFP-DYN-1^{END} rescues persistent lobe defects of *dyn-1* mutant embryos (arrowhead, debris). (j) FRAP of persistent lobes in *dyn-1* mutant embryos (recovery in 16/16 embryos, compared with 4/11 *dyn-1; dyn-1(+)* embryos from 3 independent experiments); photobleached region is dashed. Scale bars, 5 μ m. Asterisks mark PGC cell body.

co-localized at a subset of lobe necks (Fig. 6b). Because our light-sheet imaging experiments indicated that all lobe necks accumulate actin and dynamin before scission, these findings suggest that the two proteins localize to lobe necks sequentially, with a period of overlap, similar to what has been observed during clathrin-mediated vesicle endocytosis in mammalian cells³¹. In *Ist-4(RNAi)* embryos examined at a single time point during the 3-fold stage, nearly all lobe necks failed to accumulate YFP-DYN-1^{END} and CFP-ACT-5^{END} (Fig. 6d). By contrast, YFP-LST-4^{END} accumulated normally in *ced-10* mutants (Fig. 6e). We conclude that LST-4 promotes actin and dynamin accumulation at lobe necks, and propose that all three proteins operate together or sequentially within endodermal cells to mediate lobe scission. Since CED-10 is dispensable for dynamin and LST-4 localization, it functions in a distinct manner to induce actin accumulation (Fig. 6f).

DISCUSSION

Our findings reveal an unexpected role for endoderm in remodelling the size and contents of primordial germ cells during development. The presence of mitochondria and P granules in PGC lobe debris suggests that lobes may function as a receptacle that PGCs use to discard unwanted organelles and other cytoplasmic components, preparing the cells for their impending transition to become germline stem cells during larval stages. In particular, we observed a striking loss in PGC mitochondria, which contained high levels of oxidants relative to mitochondria in most other embryonic cells. Therefore, one role for PGC lobe cannibalism by endoderm may be to protect PGCs from damage caused by mitochondrial oxidants. We speculate that elimination of most PGC mitochondria may be particularly important for embryos that hatch in the absence of food—a diapause-like state

in which larvae can remain for several weeks³². PGCs are dormant during this period, but when they are genetically forced to divide, on re-feeding, worms often develop into sterile adults³³. Intriguingly, treatment with the mitochondrial translation inhibitor doxycyclin can prevent sterility in this situation³⁴, suggesting that mitochondrial activity is normally regulated in PGCs to ensure their health. Regardless of the role for PGC lobe elimination, our findings provide an additional example of the large-scale segregation of organelles or cytoplasmic components into and out of germ cells. Other examples include the pumping of cytoplasmic contents and organelles from support germ cells into enlarging oocytes in worms, flies and mice^{35–37}, and the scuttling of cytoplasmic components that is needed to produce streamlined spermatozoa³⁸. Thus, while cytoplasmic remodelling is a conserved feature of germ cells undergoing gametogenesis, our findings show that it can also occur in primordial germ cells.

Although PGCs can form lobes autonomously, our experiments suggest that endodermal cells may be uniquely able to remove PGC lobes. For example, when endodermal cells are missing, PGCs form lobes that accumulate between the cell bodies rather than embed into other cells (see Fig. 3h), and we have not observed PGC debris within other cell types. These findings raise the possibility that a specialized adhesion or recognition mechanism exists to ensure that PGC lobes embed specifically into endodermal cells. PGCs and endodermal cells may also signal to each other to initiate lobe removal, since lobes remain embedded for an extended period before they are removed, but are always removed during a relatively short developmental window. In addition, our observation that all lobes from one PGC are removed before any lobes from the other PGC are removed suggests the presence of intercellular signals that coordinate lobe scission.

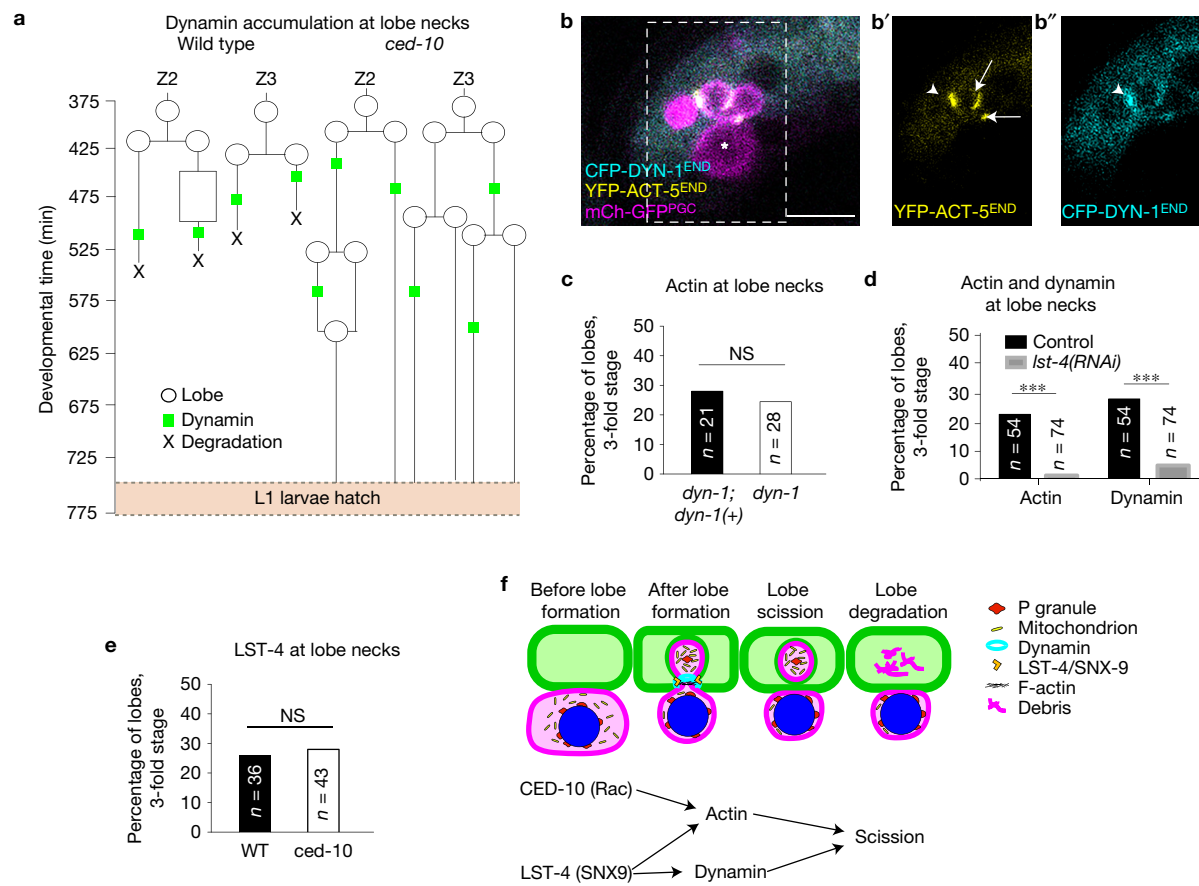


Figure 6 A pathway for lobe scission. (a) Pedigree of lobes and dynamin localization at lobe necks in wild-type and *ced-10* mutant embryos. (b–b'') Co-localization of YFP-ACT-5^{END} and CFP-DYN-1 at lobe necks; arrowhead denotes co-localization whereas arrows point to lobes that are marked predominantly by YFP-ACT-5^{END}. b' and b'' are magnifications of the outlined area in b. (c) Quantification of actin localization in *dyn-1* rescued embryos and *dyn-1* mutant embryos (NS, not significant, Fisher's exact test; data shown from 2 independent experiments). (d) Quantification of actin and dynamin localization at lobe necks in

control and *Ist-4(RNAi)* 3-fold embryos (**P < 0.001, Fisher's exact test; data shown from 4 independent experiments). (e) Quantification of LST-4 localization in wild-type and *ced-10* mutant embryos (NS, not significant, Fisher's exact test; data shown from 3 independent experiments). (f) A schematic representation of lobe cannibalism. PGCs form organelle-rich lobes that embed into adjacent endodermal cells. Through a pathway outlined beneath the diagram, lobes undergo scission from PGCs and are digested within endodermal cells. Scale bar, 5 μm. Asterisks mark PGC cell body.

We propose that PGC lobes are cannibalized when CED-10 (Rac) and LST-4 (SNX9) induce the accumulation of F-actin and dynamin at lobe necks, causing the neck to narrow and undergo scission (Fig. 6f). Actin, dynamin and SNX9 accumulate at the necks of many endocytic vesicles to promote their scission^{21,31}, suggesting that they may function similarly in the two events, despite the need during PGC lobe cannibalism to resolve four membranes rather than two. Cannibalism of PGC lobes by endodermal cells occurs through a mechanism that appears distinct from cellular remodelling events involving uptake of cellular fragments. For example, photoreceptors shed their outer segments, which are phagocytosed by adjacent retinal pigment epithelial cells, and unwanted axons and dendrites in the developing nervous system fragment and are scavenged by glial cells^{39,40}. However, an active role for engulfing cells has been proposed but not conclusively demonstrated for some remodelling events, such as CNS synapse remodelling by microglia and *Drosophila* sensory axon remodelling by skin cells^{41,42}, raising the possibility that the mechanism of intercellular cannibalism we describe here may be a more widespread method used to shape and remodel cells. □

METHODS

Methods, including statements of data availability and any associated accession codes and references, are available in the online version of this paper.

Note: Supplementary Information is available in the online version of the paper

ACKNOWLEDGEMENTS

We thank the *Caenorhabditis* Genetics Center (CGC), National Bioresource Project (NBRP), and Z. Zhou (Baylor College of Medicine, USA) for providing worm strains. Caged rhodamine dextran was a gift from K. Oegema (University of California, San Diego). We thank T. Hurd (NYU School of Medicine, USA) for sharing TMRE dye and mitochondrial discussion; J. H. Choi (NYU School of Medicine, USA) for assistance in developing the technique for cell culture experiments; D. McIntyre (NYU School of Medicine, USA) for designing a nitrogen gas immobilization chamber for embryos; and L. Christiaen (New York University, USA), N. Ringstad (NYU School of Medicine, USA), T. Hurd (NYU School of Medicine, USA) and members of the Nance laboratory for comments on the manuscript. Library preparation and sequencing of genomic DNA samples was performed at the NYULMC Genome Technology Center, which is partially supported by a Cancer Center Support Grant (P30CA016087) at the Laura and Isaac Perlmutter Cancer Center. Funding was provided by the NIH (R35GM118081, R21HD084809 to J.N.), NYSTEM (C029561 to J.N.) and HHMI (J.M.H., T.-L.C.). Y.A. is an HHMI International Student Research fellow.

AUTHOR CONTRIBUTIONS

Y.A. and J.N. designed experiments. C.M. performed and analysed cell culture, MOMA-1 imaging, and *end-1 end-3* embryo experiments. Y.A. performed and analysed all other experiments, and J.H. and T.-L.C. assisted with experiments on the lattice light-sheet microscope. Y.A. and J.N. wrote the manuscript.

COMPETING FINANCIAL INTERESTS

The authors declare no competing financial interests.

Published online at <http://dx.doi.org/10.1038/ncb3439>

Reprints and permissions information is available online at www.nature.com/reprints

- Cinalli, R. M., Rangan, P. & Lehmann, R. Germ cells are forever. *Cell* **132**, 559–562 (2008).
- Seydoux, G. & Braun, R. E. Pathway to totipotency: lessons from germ cells. *Cell* **127**, 891–904 (2006).
- Molyneux, K. A., Stallock, J., Schaible, K. & Wylie, C. Time-lapse analysis of living mouse germ cell migration. *Dev. Biol.* **240**, 488–498 (2001).
- Takamura, K., Fujimura, M. & Yamaguchi, Y. Primordial germ cells originate from the endodermal strand cells in the ascidian *Ciona intestinalis*. *Dev. Genes Evol.* **212**, 11–18 (2002).
- Chihara, D. & Nance, J. An E-cadherin-mediated hitchhiking mechanism for *C. elegans* germ cell internalization during gastrulation. *Development* **139**, 2547–2556 (2012).
- DeGennaro, M. *et al.* Peroxiredoxin stabilization of DE-cadherin promotes primordial germ cell adhesion. *Dev. Cell* **20**, 233–243 (2011).
- Sulston, J. E., Schierenberg, E., White, J. G. & Thomson, J. N. The embryonic cell lineage of the nematode *Caenorhabditis elegans*. *Dev. Biol.* **100**, 64–119 (1983).
- Rohrschneider, M. R. & Nance, J. The union of somatic gonad precursors and primordial germ cells during *Caenorhabditis elegans* embryogenesis. *Dev. Biol.* **379**, 139–151 (2013).
- Owrighi, M., Broitman-Maduro, G., Luu, T., Roberson, H. & Maduro, M. F. Roles of the Wnt effector POP-1/TCF in the *C. elegans* endomesoderm specification gene network. *Dev. Biol.* **340**, 209–221 (2010).
- Strome, S. & Wood, W. B. Immunofluorescence visualization of germ-line-specific cytoplasmic granules in embryos, larvae, and adults of *Caenorhabditis elegans*. *Proc. Natl Acad. Sci. USA* **79**, 1558–1562 (1982).
- Head, B. P., Zulaika, M., Ryazantsev, S. & van der Bliek, A. M. A novel mitochondrial outer membrane protein, MOMA-1, that affects cristae morphology in *Caenorhabditis elegans*. *Mol. Biol. Cell* **22**, 831–841 (2011).
- Rolland, S. G., Lu, Y., David, C. N. & Conradt, B. The BCL-2-like protein CED-9 of *C. elegans* promotes FZO-1/Mfn1,2- and EAT-3/Opa1-dependent mitochondrial fusion. *J. Cell Biol.* **186**, 525–540 (2009).
- Yang, W. & Hekimi, S. A mitochondrial superoxide signal triggers increased longevity in *Caenorhabditis elegans*. *PLoS Biol.* **8**, e1000556 (2010).
- Chen, B. C. *et al.* Lattice light-sheet microscopy: imaging molecules to embryos at high spatiotemporal resolution. *Science* **346**, 1257998 (2014).
- Reddien, P. W. & Horvitz, H. R. CED-2/CrkII and CED-10/Rac control phagocytosis and cell migration in *Caenorhabditis elegans*. *Nat. Cell Biol.* **2**, 131–136 (2000).
- Lundquist, E. A., Reddien, P. W., Hartwig, E., Horvitz, H. R. & Bargmann, C. I. Three *C. elegans* Rac proteins and several alternative Rac regulators control axon guidance, cell migration and apoptotic cell phagocytosis. *Development* **128**, 4475–4488 (2001).
- Kinchen, J. M. *et al.* Two pathways converge at CED-10 to mediate actin rearrangement and corpse removal in *C. elegans*. *Nature* **434**, 93–99 (2005).
- Wang, X. & Yang, C. Programmed cell death and clearance of cell corpses in *Caenorhabditis elegans*. *Cell Mol. Life Sci.* **73**, 2221–2236 (2016).
- Shin, N. *et al.* SNX9 regulates tubular invagination of the plasma membrane through interaction with actin cytoskeleton and dynamin 2. *J. Cell Sci.* **121**, 1252–1263 (2008).
- Lundmark, R. & Carlsson, S. R. Sorting nexin 9 participates in clathrin-mediated endocytosis through interactions with the core components. *J. Biol. Chem.* **278**, 46772–46781 (2003).
- McMahon, H. T. & Boucrot, E. Molecular mechanism and physiological functions of clathrin-mediated endocytosis. *Nat. Rev. Mol. Cell Biol.* **12**, 517–533 (2011).
- Almendinger, J. *et al.* A conserved role for SNX9-family members in the regulation of phagosome maturation during engulfment of apoptotic cells. *PLoS ONE* **6**, e18325 (2011).
- Chen, D. *et al.* Clathrin and AP2 are required for phagocytic receptor-mediated apoptotic cell clearance in *Caenorhabditis elegans*. *PLoS Genet.* **9**, e1003517 (2013).
- Cheng, S. *et al.* PtdIns(4,5)P(2) and PtdIns3P coordinate to regulate phagosomal sealing for apoptotic cell clearance. *J. Cell Biol.* **210**, 485–502 (2015).
- Lu, N., Shen, Q., Mahoney, T. R., Liu, X. & Zhou, Z. Three sorting nexins drive the degradation of apoptotic cells in response to PtdIns(3)P signaling. *Mol. Biol. Cell* **22**, 354–374 (2011).
- Yu, X., Odera, S., Chuang, C. H., Lu, N. & Zhou, Z. *C. elegans* dynamin mediates the signaling of phagocytic receptor CED-1 for the engulfment and degradation of apoptotic cells. *Dev. Cell* **10**, 743–757 (2006).
- Lundmark, R. & Carlsson, S. R. Regulated membrane recruitment of dynamin-2 mediated by sorting nexin 9. *J. Biol. Chem.* **279**, 42694–42702 (2004).
- Soulet, F., Yarar, D., Leonard, M. & Schmid, S. L. SNX9 regulates dynamin assembly and is required for efficient clathrin-mediated endocytosis. *Mol. Biol. Cell* **16**, 2058–2067 (2005).
- Yarar, D., Waterman-Storer, C. M. & Schmid, S. L. SNX9 couples actin assembly to phosphoinositide signals and is required for membrane remodeling during endocytosis. *Dev. Cell* **13**, 43–56 (2007).
- Badour, K. *et al.* Interaction of the Wiskott-Aldrich syndrome protein with sorting nexin 9 is required for CD28 endocytosis and cosignaling in T cells. *Proc. Natl Acad. Sci. USA* **104**, 1593–1598 (2007).
- Taylor, M. J., Perrais, D. & Merrifield, C. J. A high precision survey of the molecular dynamics of mammalian clathrin-mediated endocytosis. *PLoS Biol.* **9**, e1000604 (2011).
- Baugh, L. R. To grow or not to grow: nutritional control of development during *Caenorhabditis elegans* L1 arrest. *Genetics* **194**, 539–555 (2013).
- Fukuyama, M. *et al.* *C. elegans* AMPKs promote survival and arrest germline development during nutrient stress. *Biol. Open* **1**, 929–936 (2012).
- Wolf, T., Qi, W., Schindler, V., Runkel, E. D. & Baumeister, R. Doxycyclin ameliorates a starvation-induced germline tumor in *C. elegans* *daf-18/PTEN* mutant background. *Exp. Gerontol.* **56**, 114–122 (2014).
- Wolke, U., Jezuit, E. A. & Priess, J. R. Actin-dependent cytoplasmic streaming in *C. elegans* oogenesis. *Development* **134**, 2227–2236 (2007).
- Lei, L. & Spradling, A. C. Mouse oocytes differentiate through organelle enrichment from sister cyst germ cells. *Science* **352**, 95–99 (2016).
- Cox, R. T. & Spradling, A. C. A Balbiani body and the fusome mediate mitochondrial inheritance during *Drosophila* oogenesis. *Development* **130**, 1579–1590 (2003).
- Chu, D. S. & Shakes, D. C. Spermatogenesis. *Adv. Exp. Med. Biol.* **757**, 171–203 (2013).
- Kevany, B. M. & Palczewski, K. Phagocytosis of retinal rod and cone photoreceptors. *Physiology (Bethesda)* **25**, 8–15 (2010).
- Corty, M. M. & Freeman, M. R. Cell biology in neuroscience: architects in neural circuit design: glia control neuron numbers and connectivity. *J. Cell Biol.* **203**, 395–405 (2013).
- Schafer, D. P. *et al.* Microglia sculpt postnatal neural circuits in an activity and complement-dependent manner. *Neuron* **74**, 691–705 (2012).
- Han, C. *et al.* Epidermal cells are the primary phagocytes in the fragmentation and clearance of degenerating dendrites in *Drosophila*. *Neuron* **81**, 544–560 (2014).

METHODS

Strains. *C. elegans* strains were maintained as previously described. References for mutant alleles listed below can be found at Wormbase (www.Wormbase.org). The following strains were used: N2 (wild type), FT834: *xnSi13* [*Pmex-5::gfp-PH::tbb-2^{3'UTR}*, *unc-119(+)*]; *zuls244* [*Pnmy-2::pgl-1::mRFP*, *unc-119(+)*]⁵, FT1016: *xnIs360* [*Pmex-5::mCherry-PH::nos-2^{3'UTR}*, *unc-119(+)*]⁸ *zuls70* [*Pend-1::gfp::caax*, *unc-119(+)*]⁴³, FT1214: *ced-10(n1993)*; *xnIs360 zuls70*, FT1259: *ced-5(n1812)*; *xnIs360 zuls70*, FT1262: *ced-3(n171)*; *xnIs360 zuls70*, FT1303: *ced-7(n1892)*; *xnIs360 zuls70*, FT1314: *ced-2(e1752)*; *xnIs360 zuls70*, FT1372: *lin-2(e1309)*; *xnIs360 zuls70*, FT1407: *xnEx326* [*Pend-1::yfp::act-5*, *pRF4*]; *xnIs360*, FT1408: *ced-7(n1892)*; *ced-5(n1812)*; *xnIs360 zuls70*, FT1436: *xnEx338* [*Pend-1::yfp::dyn-1*, *pRF4*]; *xnIs360*, FT1468: *lst-4(xn45)*; *lin-2(e1309)*; *xnIs360*, FT1527: *ced-10(n1993)*; *xnIs360*; *xnEx375* [*Pend-1::ced-10^{3'UTR}*, *Psur-5::gfp*], FT1538: *xnSi45* [*Pmex-5::mCherry::moma-1::nos-2^{3'UTR}*, *unc-119(+)*]; *xnIs360* [*Ppie-1::gfp-PH*; *unc-119(+)*], FT1554: *end-1(ok558)* *end-3(ok1448)*; *irEx568* [*end-1(+)*; *end-3(+)*; *Psur-5::dsRed*]⁹; *xnSi1* [*Pmex-5::gfp-PH::nos-2^{3'UTR}*, *unc-119(+)*]⁵, FT1619: *xn45*; *xnIs360*; *xnEx394* [*lst-4(+)*, *sur-5::gfp*], FT1630: *ced-10(n1993)*; *xnIs360*; *xnEx326*, FT1631: *ced-10(n1993)*; *xnIs360*; *xnEx338*, FT1658: *dyn-1(en9)*; *xnIs360 zuls70*; *enEx21* [*dyn-1(+)*; *Pegl-13::gfp*]²⁶, FT1659: *ced-10(tm597)*; *xnIs360*; *xnEx413* [*ced-10(+)*; *Psur-5::gfp*], FT1678: *xnSi1*; *nrf-5(sa513)*, FT1694: *pwl50* [*Plmp-1::lmp-1::gfp*]⁴⁴; *xnIs360*, FT1697: *ttr52(tm2078)*; *xnIs360 zuls70*, WM186: *avr-1(ad1302)*; *Mos1(ttTi5605)*; *unc-119(ed3)*; *glc-1(pk54:Te1)* *avr-15(ad1051)*⁴⁵, RT476: *pwl170* [*Pvha6::gfp::rab-7*]⁴⁶, FT1778: *xnIs360*; *xnEx450* [*Pend-1::yfp::act-5*, *Pend-1::cfp::dyn-1*, *pRF4*], FT1780: *lst-4(xn45)*; *xnIs360*; *xnEx452* [*Pend-1::lst-4::yfp*, *pRF4*], FT1787: *ced-1(e1735)*; *xnIs360 zuls70*, FT1829: *dyn-1(en9)*; *xnIs360*; *enEx21* [*dyn-1(+)*; *Pegl-13::gfp*]; *xnEx464* [*Pend-1::yfp::act-5*, *pRF4*].

Fusion protein nomenclature in the text and figures relates to the following transgenes: mCh-Mem^{PGC}: *xnIs360* [*Pmex-5::mCherry-PH::nos-2^{3'UTR}*, *unc-119(+)*], GFP-Mem^{END}: *zuls70* [*Pend-1::gfp::caax*, *unc-119(+)*], LMP-1-GFP: *pwl50* [*Plmp-1::lmp-1::gfp*], PGL-RFP: *zuls244* [*Pnmy-2::pgl-1::mRFP*, *unc-119(+)*], mCh-MOMA-1^{PGC}: *xnSi45* [*Pmex-5::mCherry::moma-1::nos-2^{3'UTR}*, *unc-119(+)*], GFP-Mem^{ALL}: *itIs38* [*Ppie-1::gfp-PH*, *unc-119(+)*], GFP-Mem^{PGC}: *xnSi1* [*Pmex-5::gfp-PH::nos-2^{3'UTR}*, *unc-119(+)*], GFP-RAB-7: *pwl170* [*Pvha6::gfp::rab-7*], YFP-ACT-5^{END}: *xnEx326* [*Pend-1::yfp::act-5*, *pRF4*], LST-4-YFP^{END}: *xnEx452* [*Pend-1::lst-4::yfp*, *pRF4*], YFP-DYN-1^{END}: *xnEx338* [*Pend-1::yfp::dyn-1*, *pRF4*], YFP-ACT-5^{END} with CFP-DYN-1^{END}: *xnEx450* [*Pend-1::yfp::act-5*, *Pend-1::cfp::dyn-1*, *pRF4*].

RNAi. *lst-4* RNAi experiments were performed using the bacterial feeding method, as described, using clone Y37A1B.2 from the Ahringer RNAi Library⁴⁷; empty vector (pPD129.36) was used as a negative control. L3/L4 worms grown on OP50 on NGM plates were washed and placed on RNAi plates seeded with HT115 transformed with feeding plasmids. Worms were allowed to feed for 36–48 h at 20 °C before phenotypes were scored in progeny.

Mutagenesis screen. EMS was used in an unbiased chemical mutagenesis screen for maternal-effect mutations affecting PGC lobe scission or degradation, following a previously described mutagenesis protocol⁴⁸. Strain FT1372 was used for mutagenesis. The *lin-2(e1309)* mutation prevents vulva formation in most worms, and hermaphrodites accumulate hatched eggs inside the uterus. F3 L1 larvae within the uterus of F2 hermaphrodites were screened on slides using a Zeiss Axiolmager, 40× 1.3 NA objective, EXFO illumination and a Cy3 filter set. L1 larvae with persistent PGC lobes and a superficially normal intestine were recovered. The *lst-4(xn45)* mutation was recovered from the screen and was outcrossed to strain FT1016 three times prior to phenotypic analysis.

Whole-genome sequencing and mutation identification. Genomic DNA from *xn45* homozygotes was isolated using the Puregene Core Kit A (Qiagen), followed by three series of phenol/chloroform extraction. Genomic DNA libraries were constructed and bar-coded using the Kapa library preparation kit (KAPA BIOSYSTEMS), and samples were sequenced using an Illumina HiSeq 2500 Sequencer in 100 bp paired-end reads. Sequencing data were uploaded and processed using a CloudMap Unmapped workflow (www.usegalaxy.org)⁴⁹. Genome Annotation Tool Kit (GATK) was used to annotate the variant call list. SAM files generated on www.usegalaxy.org were uploaded into Integrative Genomics Viewer to browse alignments^{50,51}.

The *lst-4(xn45)* mutation was confirmed as causative using RNAi phenocopy and transformation rescue, as shown in Supplementary Fig. 5. For transformation rescue, genomic DNA encompassing the *lst-4* gene with 1.3 kb of upstream and 0.9 kb of downstream sequence (primers: 5'-gacgaacagagacagcaaaa-3' and 5'-aaggtgttaggag gtcggtg-3') was microinjected into FT1619 *lst-4(xn45)*; *xnIs360* worms, using *sur-5::gfp* as a co-transformation marker. Two independent transgenic lines were scored, and both rescued the persistent lobe phenotype. Data for transgenic array *xnEx394* are shown in Supplementary Fig. 5a.

Transgene construction. Transgenes *Pend-1::yfp::act-5*, *Pend-1::cfp::act-5*, *Pend-1::yfp::dyn-1*, *Pend-1::cfp::dyn-1*, *Pmex-5::mCherry::moma-1::nos-2^{3'UTR}*, *Pend-1::ced-10::ced-10^{3'UTR}*, *Pend-1::lst-4::mCardinal* and *Pend-1::lst-4::yfp* were created using Gibson assembly⁵². Briefly, overlapping primers were used to assemble the *end-1* promoter sequence, a fluorescent tag and *act-5*, *dyn-1*, *lst-4*, *moma-1* cDNA or *ced-10* gDNA into a plasmid. *end-1* promoter⁵³ and *yfp* or *cfp* were amplified together from *pJN584* and *pJN583* respectively. *act-5* and *dyn-1* isoform a were amplified from cDNA and cloned 3' to *yfp* or *cfp*.

For *Pend-1::yfp::act-5* and *Pend-1::cfp::act-5*, the following homology arms were used to fuse *act-5* to *yfp* and *cfp*:

```
5'-ctggattacacatggcatggatgaactatacaaaaggagcctggaagaagaatcgcgcc-3'
5'-gtaatgtagcgcaccggcgctcagttggaattctacgaatgtagaagcattcgggtgaacaat-3'
```

For *Pend-1::yfp::dyn-1* and *Pend-1::cfp::dyn-1*, the following homology arms were used to fuse *dyn-1* to *yfp* and *cfp*:

```
5'-gctggattacacatggcatggatgaactatacaaaaggagcctgctggtgcaaaaccaggga-3'
5'-gtaatgtagcgcaccggcgctcagttggaattctacgaatgtagaagcattcgggtgcaatgtt-3'
```

For *Pmex-5::mCherry::moma-1::nos-2^{3'UTR}*, the following homology arms were used to replace *PH* sequence with *moma-1* cDNA in *Pmex-5::mCherry-PH::nos-2^{3'UTR}*:

```
5'-ccatctgccatcgtcaaaactcctgagccaccgaaataaaaaccagcttcttcta-3'
5'-tgtctccacaatcgctgtctgtctgctacgctccgctcccttatacaatcatcatgcc-3'
```

For *Pend-1::ced-10::ced-10^{3'UTR}*, the *ced-10* genomic sequence was amplified and inserted into *Pend-1::yfp::act-5*, replacing *yfp::act-5* with the following homology arms:

```
5'-aacatttcaggaggacccttgagggtaccggtagaaaaatgcaagcgaatcaaatgtgt-3'
5'-gtaatgtagcgcaccggcgctcagttggaattctacgaatgaaatatacatcatcatta-3'
```

For *Pend-1::lst-4::mCardinal*, *lst-4c* isoform cDNA was inserted into *Pend-1::mCardinal* using the homology arms:

```
5'-gaagtggcgaccaagctgactcattagcctgtagatgatggggcccaatggtgagcaaggcgaggagc-3'
```

```
5'-ttgactttgaaatcactcctgcttccactgagccattaccgtaccctcaagggtcc-3'
```

For *Pend-1::lst-4::yfp*, *mCardinal* was replaced with *yfp* in *Pend-1::lst-4::mCardinal* using the homology arms:

```
5'-gcgaccaagctgactcattagcctgtagatgatggggcccaatgagtaagagaagaacttttc-3'
5'-gttagtatgagaaagttaactcaacttctcgaatgtattttagtatgttcatcatgcatc-3'
```

Worm transformation. *Pmex-5::mCherry::moma-1::nos-2^{3'UTR}* was microinjected into WM186 worms to create a chromosomal insertion using the MosSCI method⁵⁴, with modifications as described⁵⁵.

Pend-1::yfp::act-5, *Pend-1::yfp::dyn-1*, *Pend-1::cfp::dyn-1*, *Pend-1::ced-10::ced-10^{3'UTR}*, *Pend-1::cfp::caax*, *Pend-1::lst-4::mCardinal*, genomic *lst-4(+)* and *Pend-1::lst-4::yfp* were microinjected together with either *rol-6(su1006)* or *Psur-5::gfp* (see the Strains section) into young adult worms to create transmitting extrachromosomal arrays⁵⁶.

Cell culture. Embryonic cells were isolated from strain FT1703 as described previously⁵⁷, except the chitinase treatment step was eliminated. Cells (200–500 µl) resuspended in embryonic culture medium were pipetted onto MatTek dishes (35 mm Glass Bottom Dishes No. 1.0) coated with poly-L-lysine. Cells were allowed to settle to the bottom of the dish for approximately 10 min before imaging as described below. The time from worm isolation to cell imaging was approximately 1.5 h.

Mitochondrial dye experiments. Dyes were introduced into *C. elegans* embryos either through feeding (TMRE (Molecular Probes), a gift from R. Lehmann and T. Hurd (NYU School of Medicine, USA))—or by perforating the eggshell and vitelline membrane with a laser (MitoSOX (Molecular Probes) and MitoTracker Green FM (Molecular Probes)). For feeding, 20 µl of 10 µM TMRE was placed on OP50-seeded NGM plates and allowed to soak in. L4 worms were moved to treated plates and allowed to feed for 15 h before F1 embryos and L1s were collected for imaging. For incorporation of MitoSOX and MitoTracker Green FM, embryos were collected on poly-L-lysine-coated coverslips and mounted over slides with embryonic culture media⁵⁷ containing 5 µM dye. Holes in the eggshell and vitelline membrane were made on a Zeiss Axiolmager using a 100× 1.3 NA objective and MicroPoint laser with Coumarin dye cell by aiming at the polar body. Embryos were left for one hour for equilibration of dye before imaging.

Microscopy and image analysis. *Imaging of live embryos and L1 larvae.* Embryos or L1 larvae were mounted on 4% agar pads; L1 larvae were immobilized prior to imaging using 1 mM levamisole in M9. Samples were imaged on a Leica SP5II confocal microscope, using a 63× 1.2 NA water-immersion objective lens, and HyD detectors; or alternatively on a Zeiss Axiolmager using either 40× 1.3 NA or 63× 1.4 NA objectives and an Axiocam MRM camera. Long-term time-lapse images used to create lobe pedigrees were collected on a lattice light-sheet microscope. Embryos were staged and mounted on poly-L-lysine-coated coverslips

and submerged in water during imaging. Time-lapse images were acquired as described previously¹⁴, using 488 nm and 589 nm lasers to excite YFP and mCherry, respectively. Beginning at bean stage, Z stacks (400 nm steps) were collected through the volume of the embryo every minute until embryos hatched. Image stacks were deskewed and deconvolved as described previously¹⁴.

To determine PGC volume, Z-stacks were collected on the confocal microscope, and Volocity Imaging Analysis software (Perkin Elmer) was used to integrate PGC volume. A region of interest (ROI) was drawn along the PGC membrane after noise subtraction. The volume of the cell body or of the cell body plus lobes was measured, as indicated in the figure legends.

For FRAP experiments, live embryos mounted on agar were immobilized by perfusing the slide chamber with nitrogen gas, whereas live L1 larvae were immobilized using 10 mM sodium azide. FRAP experiments were carried out on a Leica SP5II confocal microscope, using a 63× 1.2 NA water-immersion objective lens, HyD detectors, and the FRAP module. Three pre-bleach images were collected at three-second intervals. Whole lobes were selectively photobleached at 100% 594 nm laser power using the ROI tool with five successive pulses. During some FRAP experiments, a single bleaching included multiple lobes. Post-bleach images were collected at ten-second intervals for three minutes. Area bleached was measured for recovery and analysed in ImageJ (NIH) using the FRAP plugin⁵⁶. Lobes with recovery of less than 8% were classified as unrecovered, whereas lobes with recovery greater than 20% were classified as recovered. To confirm that recovery could not arise from new protein synthesis over the imaging time period, PGCs plus lobes were photobleached in their entirety in a set of control FRAP experiments. In these experiments, we observed no recovery (average recovery $4.87 \pm 1.6\%$, min = 1.76%, max = 6.82%, $n=12$).

For caged rhodamine dextran experiments, a 10,000 molecular weight dextran conjugate of CMNCBZ-caged carboxy-Q-rhodamine (a gift from K. Oegema) was injected into adult gonads as previously described⁵⁹. Embryos were dissected from injected animals after 5 h at 20 °C and allowed to develop in egg salts until hatching. Newly hatched L1 larvae were immobilized with 10 mM NaN₃ and mounted on agar pads. Photoactivation experiments were carried out using a Leica SP5 II confocal microscope, 63× 1.2 NA water-immersion objective lens, and HyD detectors. Two pre-photoactivation images were collected at two-second intervals. Dye within a portion of a single PGC cell body was selectively uncaged with three pulses of 405 nm laser at 25% power. Uncaged rhodamine dextran was imaged every two seconds in a single plane using a 561 nm laser.

PGC mitochondrial volume was quantified by using Volocity (Perkin Elmer) to measure the volume occupied by mCh-MOMA-1^{PGC} or TMRE dye in mid-staged embryos and L1 larvae.

PGC debris count was quantified on Volocity Imaging Analysis software (Perkin Elmer). Briefly, a ROI was defined above the PGCs and within the endodermal cells. The software was instructed to find objects in the red channel with a minimum size of 0.01 μm³ but less than 5 μm³. Number of objects found was used as number of debris count.

PGC mitochondrial dye intensity was measured on Volocity (Perkin Elmer). Normalized intensity levels were calculated as the average fluorescent intensity in PGCs divided by the average fluorescent intensity in the embryonic soma.

The 3D model of PGCs and endoderm (Supplementary Video 2) was rendered from fluorescent images acquired on a Leica SP5 II confocal microscope. Images were used to create contours in trakEM2 on ImageJ (NIH). Contour files were exported as .OBJ files and imported into the 3D graphics and animation software Blender (open source) for final 3D rendering.

The schematic of endodermal cell lineage was based on ref. 60.

Imaging fixed embryos. To examine YFP-ACT-5^{END} and CFP-DYN-1^{END} localization in *ced-10* mutants and *lst-4(RNAi)*, embryos were fixed in 3.7% formaldehyde within egg salts (50 mM PIPES, 25 mM HEPES, 10 mM EGTA, and 2 mM MgCl₂) for ten minutes. Fixed embryos were washed with PBST, mounted on agar pads, and imaged on a confocal microscope as described above. Z-stacks (600 nm step size) were acquired through the volume of the PGCs.

Imaging cultured cells. Cells in MatTek dishes were imaged using a 40× 0.8 NA dipping lens on a Leica SP5II confocal microscope, illuminating with the 594 nm laser at 50% power. Z-stacks (8 planes, 1.85 μm step size) of cells were imaged every 30 min.

Statistical and reproducibility. Categorical data, such as recovery versus no recovery in FRAP experiments, and presence or absence of actin at lobe necks, was analysed

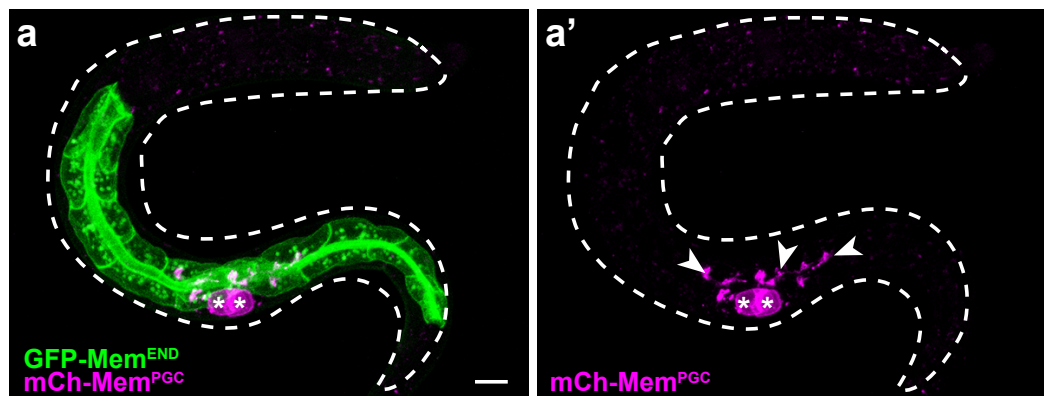
by building contingency tables and using Fisher's exact test to determine *P* values. For normally distributed data, such as PGC volume or particles of PGC debris, two-tailed *t*-tests (paired and unpaired) were used to analyse the degree of difference between two experimental groups. Data are presented as mean ± standard deviation (s.d.), as indicated. *P* values are indicated, and 'not significant' (NS) was defined as *P* > 0.05. The s.d. of compared groups was not assumed to be the same; hence, unpaired *t*-tests were performed using Welch's correction. For experiments analysing protein accumulation at individual lobes, sample units (*n*) were the number of lobes analysed (number of embryos is indicated). For all other experiments, the number of sample units (*n*) represents number of embryos or larvae, from a minimum of two independent experiments for statistical analysis.

The research subjects used in this study were hermaphrodite *C. elegans* embryos and L1 larvae in controlled laboratory experiments. A minimum sample size of ten was selected for reliable analysis of experiments, except for lattice light-sheet microscope time-lapse experiments, where six embryos were imaged for each condition. Power analysis was not used to calculate sample size. With the exception of lattice light-sheet experiments and experiments to demonstrate the feasibility of the FRAP assay (Fig. 3c), all experiments were repeated two or more times to validate results. During data collection, only damaged embryos were excluded from data. Outliers were not defined prior to experiments or excluded from analysis. Experiments were not randomized and were not performed blind.

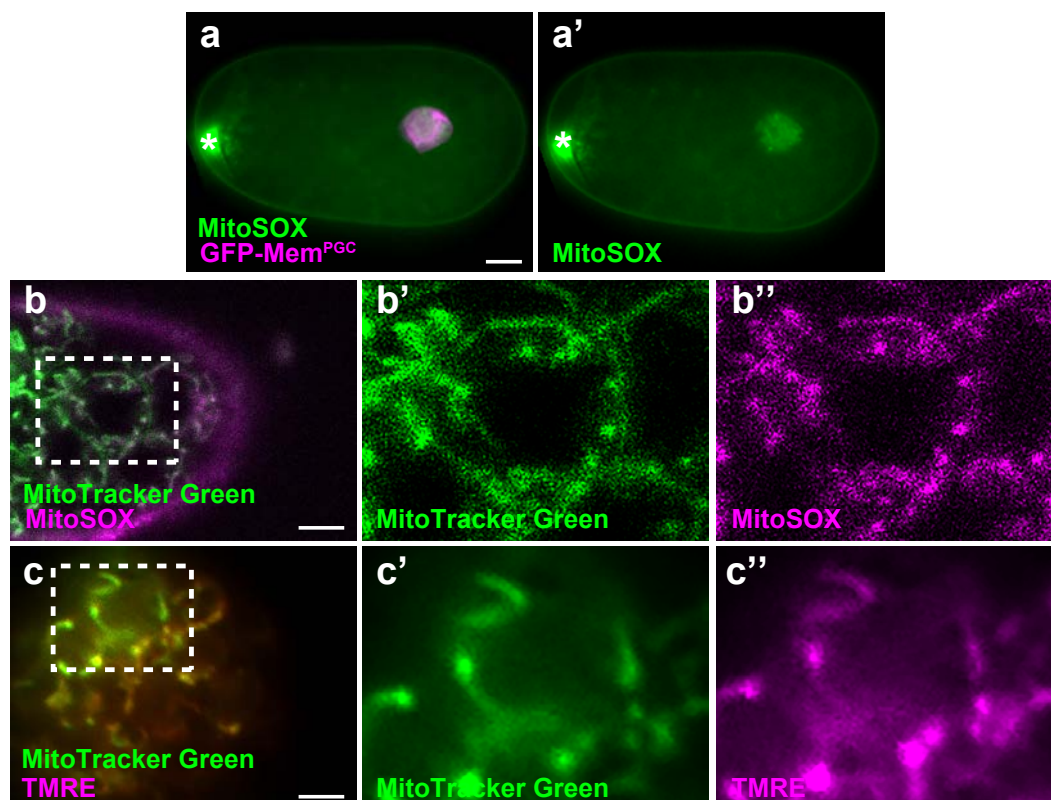
Data availability. Whole-genome sequencing data for *xnr45* has been deposited on SRA (NCBI) under the accession number SRP078084, and can be accessed through the link: <http://trace.ncbi.nlm.nih.gov/Traces/sra/?run=SRR3750603>.

43. Wehman, A. M., Poggioli, C., Schweinsberg, P., Grant, B. D. & Nance, J. The P4-ATPase TAT-5 inhibits the budding of extracellular vesicles in *C. elegans* embryos. *Curr. Biol.* **21**, 1951–1959 (2011).
44. Treusch, S. *et al.* *Caenorhabditis elegans* functional orthologue of human protein h-mucopolipin-1 is required for lysosome biogenesis. *Proc. Natl Acad. Sci. USA* **101**, 4483–4488 (2004).
45. Shirayama, M. *et al.* piRNAs initiate an epigenetic memory of nonself RNA in the *C. elegans* germline. *Cell* **150**, 65–77 (2012).
46. Chen, C. C. RAB-10 is required for endocytic recycling in the *Caenorhabditis elegans* intestine. *Mol. Biol. Cell* **17**, 1286–1297 (2006).
47. Kamath, R. S., Martinez-Campos, M., Zipperlen, P., Fraser, A. G. & Ahringer, J. Effectiveness of specific RNA-mediated interference through ingested double-stranded RNA in *Caenorhabditis elegans*. *Genome Biol.* **2**, RESEARCH0002 (2001).
48. Brenner, S. The genetics of *Caenorhabditis elegans*. *Genetics* **77**, 71–94 (1974).
49. Minevich, G., Park, D. S., Blankenberg, D., Poole, R. J. & Hobert, O. CloudMap: a cloud-based pipeline for analysis of mutant genome sequences. *Genetics* **192**, 1249–1269 (2012).
50. Robinson, J. T. *et al.* Integrative genomics viewer. *Nat. Biotechnol.* **29**, 24–26 (2011).
51. Thorvaldsdottir, H., Robinson, J. T. & Mesirov, J. P. Integrative Genomics Viewer (IGV): high-performance genomics data visualization and exploration. *Brief Bioinform.* **14**, 178–192 (2013).
52. Gibson, D. G. *et al.* Enzymatic assembly of DNA molecules up to several hundred kilobases. *Nat. Methods* **6**, 343–345 (2009).
53. Nance, J., Munro, E. M. & Priess, J. R. *C. elegans* PAR-3 and PAR-6 are required for apicobasal asymmetries associated with cell adhesion and gastrulation. *Development* **130**, 5339–5350 (2003).
54. Frokjaer-Jensen, C. *et al.* Single-copy insertion of transgenes in *Caenorhabditis elegans*. *Nat. Genet.* **40**, 1375–1383 (2008).
55. Armenti, S. T., Chan, E. & Nance, J. Polarized exocyst-mediated vesicle fusion directs intracellular lumenogenesis within the *C. elegans* excretory cell. *Dev. Biol.* **394**, 110–121 (2014).
56. Mello, C. C., Kramer, J. M., Stinchcomb, D. & Ambros, V. Efficient gene transfer in *C. elegans* extrachromosomal maintenance and integration of transforming sequences. *EMBO J.* **10**, 3959–3970 (1991).
57. Strange, K., Christensen, M. & Morrison, R. Primary culture of *Caenorhabditis elegans* developing embryo cells for electrophysiological, cell biological and molecular studies. *Nat. Protoc.* **2**, 1003–1012 (2007).
58. Lynch, A. M. *et al.* A genome-wide functional screen shows MAGI-1 is an L1CAM-dependent stabilizer of apical junctions in *C. elegans*. *Curr. Biol.* **22**, 1891–1899 (2012).
59. Green, R. A. *et al.* The midbody ring scaffolds the abscission machinery in the absence of midbody microtubules. *J. Cell Biol.* **203**, 505–520 (2013).
60. Fukushige, T., Goszczynski, B., Yan, J. & McGhee, J. D. Transcriptional control and patterning of the *pho-1* gene, an essential acid phosphatase expressed in the *C. elegans* intestine. *Dev. Biol.* **279**, 446–461 (2005).

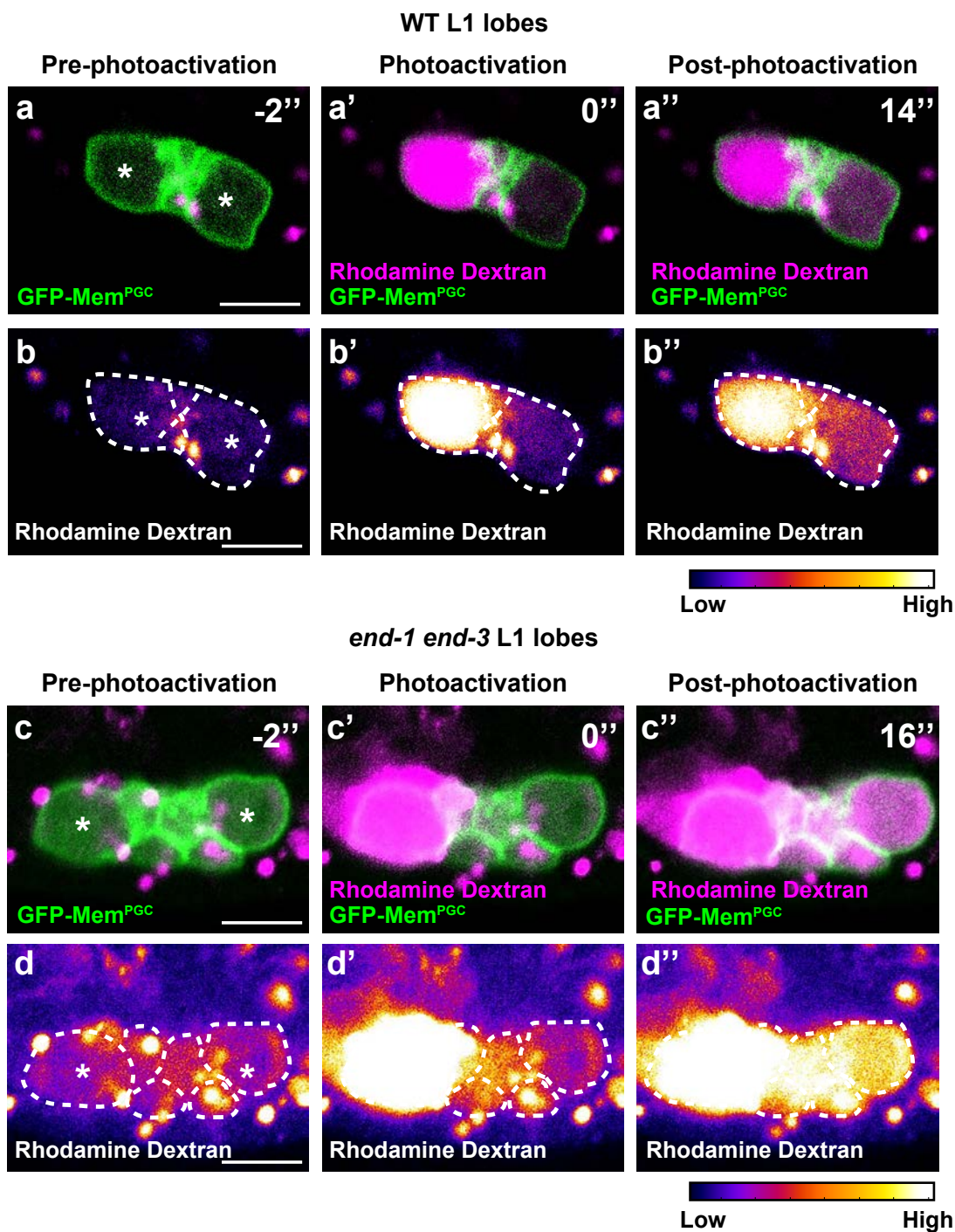
DOI: 10.1038/ncb3439



Supplementary Figure 1 PGC lobe digestion by endoderm. (a-a') A newly hatched L1 larva (body outlined). PGC debris (arrowheads) can be seen inside endodermal cells (intestinal rings V and VI). Scale bar, 5 μ m.

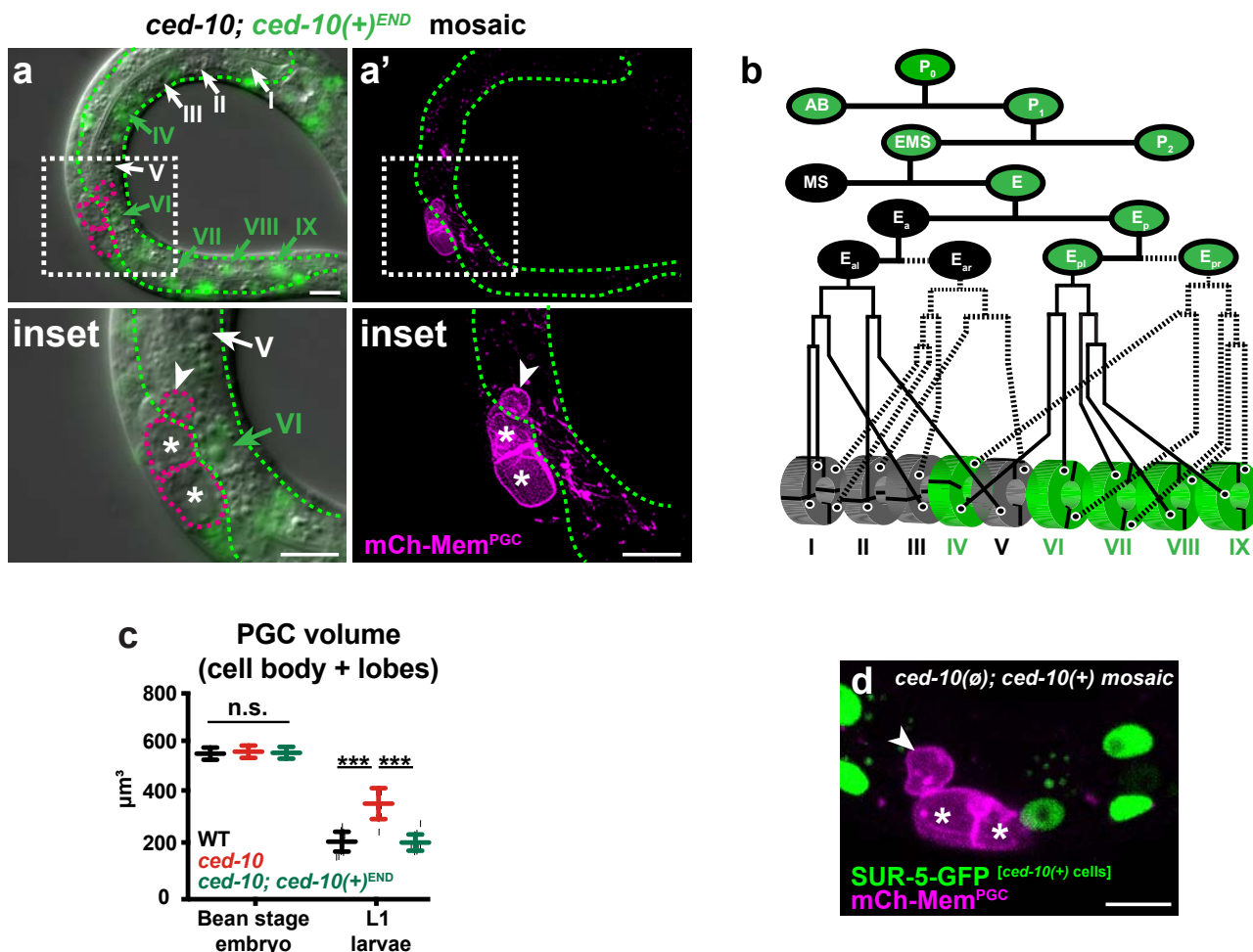


Supplementary Figure 2 Characterization of mitochondrial dyes. (a-a') MitoSOX shows stronger labeling in PGCs (one shown, magenta) compared to most somatic cells in the embryo. Asterisk denotes dye accumulation at hole made in eggshell to introduce dye. (b) MitoTracker Green (b') and MitoSOX (b'') colocalize in embryonic mitochondria. (c) MitoTracker Green (c') and TMRE (c'') colocalize to mitochondria in embryonic mitochondria. Scale bar, 5 μ m.



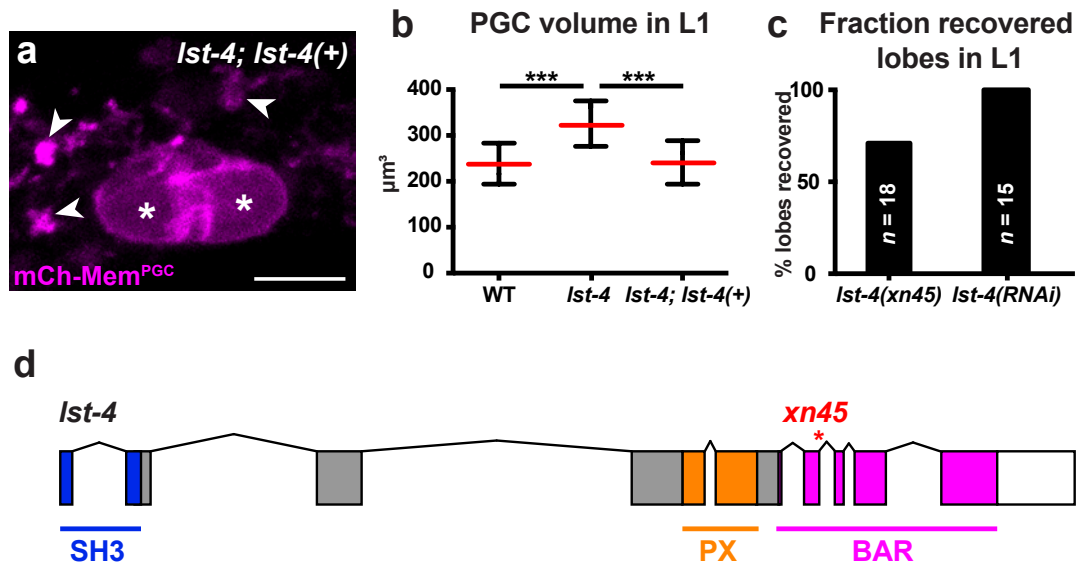
Supplementary Figure 3 Rhodamine Dextran diffusion from cell bodies into lobes. (a-b'') Photoactivation of caged Rhodamine Dextran in wild-type L1 larva. Photoactivation in a single PGC (a', b') is followed by diffusion into the adjacent PGC (PGCs are connected by a cytoplasmic bridge) (a'', b'', 9/9 embryos). (c-d'') Photoactivation of caged Rhodamine

Dextran in *end-1 end-3* L1 larva. Photoactivation in a single PGC (c', d') is followed by diffusion into persistent lobes and the adjacent PGC (c'', d'', 8/8 embryos). Some caged Rhodamine Dextran becomes uncaged independently of photoactivation, and is visible as stable bright spots in the pre-photoactivation channel. Scale bar, 5µm.



Supplementary Figure 4 *ced-10* in lobe scission. (a-a') *ced-10(n1993)* mutant L1 larva with mosaic rescue by *ced-10(+)^{END}*. The rescuing *ced-10(+)^{END}* extrachromosomal array, which also expresses nuclear SUR-5-GFP, was lost in the *E_a* endodermal lineage [inset; lost in cells of intestinal ring V (white arrow), and retained in cells of intestinal ring VI (green arrow)]. (b) Schematic of endodermal cell lineage with placements of cells in intestinal rings shown below and reflecting the mosaic pattern seen in (a); adapted from 60. Green cells indicate cells with rescue array while grey cells represent loss of array. Two mosaics were found with this loss pattern, and both mosaics showed persistent lobes in intestinal ring V (white arrowhead

in inset) and lobe debris in intestinal ring VI. 11/11 intestinal mosaic L1 larvae had persistent lobes. (c) Quantification of PGC volume (cell body + lobes) in wild type, *ced-10* mutants and *ced-10(+)^{END}* (WT, n=14 embryos/L1 larvae; *ced-10* mutants, n=14 embryos/L1 larvae; *ced-10(+)^{END}*, n=14 embryos/L1 larvae. ***p < 0.001, Student's t-test, mean ± SD). Data shown is from a single independent experiment. Source data for repeat experiments is provided in Supplementary Table 3. (d) *ced-10(tm597)* null mutant L1 larva with mosaic rescue *ced-10ALL*. Rescue is lost in the intestinal ring V, where a PGC lobe persists (arrowhead). 32/32 intestinal mosaic L1 larvae had persistent lobes. Scale bar, 5μm.



Supplementary Figure 5 *Ist-4* in lobe scission. (a) *Ist-4(+)* rescue of persistent lobes in *Ist-4(xn45)* mutants; arrowheads point to lobe debris (4/4 extrachromosomal arrays completely rescued persistent lobes, n=13-28 L1 larvae examined per array). (b) Quantification of PGC volume (cell body + lobes) in L1 larvae of *Ist-4(xn45)* mutants (n=10 L1 larvae) and *Ist-4(xn45)* mutants with *Ist-4(+)* (n=10 L1 larvae), ***p < 0.001, Student's t-test, mean ± SD. Data shown is from a single independent experiment. Source data for repeat experiments is

provided in Supplementary Table 3. (c) Percent recovered lobes in FRAP experiment on persistent lobes in *Ist-4(xn45)* (n=18 L1 larvae) and *Ist-4* (RNAi) (n=18 L1 larvae) L1 larvae. (d) *Ist-4* gene structure (isoform c, Wormbase WS252). Gray rectangles are coding exons, white rectangle is the 3' UTR, and chevrons are introns. Regions of the gene encoding the SH3, PX and BAR domains are indicated. The *xn45* lesion mutates a splice donor base within an intron in the region encoding the BAR domain. Scale bar, 5μm.

Supplementary Table and Video Legends

Supplementary Table 1 Cell corpse engulfment genes and PGC lobe cannibalism. *All alleles are putative null alleles except *ced-10*(n1993) and *lst-4*(xn45), which are hypomorphic. All strains include the *xnIs360* or *xnSi1* transgenes to visualize PGC membranes. ‡Number of persistent corpses in the pharynx of L1 (Average +/- SD) ¶Percent of L1 with at least one persistent PGC lobe embedded in endoderm

Supplementary Table 2 *dyn-1* and PGC lobe cannibalism. *All strains include the *xnIs360* transgene to visualize PGC membranes. The *dyn-1*(+) extrachromosomal array is *enEx21*. ‡No embedded lobes remained. Debris within intestinal cells ¶¶Some embedded lobes and some debris within intestinal cells ¶¶Embedded lobes, and no debris within intestinal cells

Supplementary Table 3 Statistics Source Data.

Supplementary Video 1 PGC lobe formation. Embryo is oriented posterior to the left, and turns from a ventral view to a lateral view (dorsal up) as the movie progresses. PGC and endodermal cell membranes are labeled. PGC lobes ('L') begin forming ~50 minutes into the movie and embed into endodermal cells.

Supplementary Video 2 Rendering of PGC lobes embedded into endodermal cells. Rendered data from a 2-fold embryo expressing endoderm and PGC surface markers. PGCs (magenta) extend lobes into adjacent endodermal cells (green).

Supplementary Video 3 Lobe formation in a cultured PGC. PGC membranes and nucleus are labeled. The nucleus moves to one side of the cell and lobe ('L') extends from the opposite side beginning at ~150 minutes into the movie.

Supplementary Video 4 P granule movement into PGC lobes. Embryo is oriented posterior to the left. Before lobe formation, all P granules (PGL-1-RFP) are found at the nuclear periphery. A P granule can be seen detaching from the nuclear periphery and moving into the lobe ('L') beginning at 42 minutes into the movie.

Supplementary Video 5 Mitochondria in PGC lobes. Embryo is oriented posterior to the left. All cell membranes are labeled with GFP (PGC membranes are brighter), and mitochondria within PGCs are labeled with mCh-MOMA-1 (green and red channels were switched). Both PGCs are initially visible, then one moves out of the focal plane. Lobe formation begins 16 minutes into the movie, and mitochondria can be seen localizing preferentially to the lobe ('L').